Geophysical Research Letters®

RESEARCH LETTER
10.1029/2025GL120870

Key Points:

- We present the first experimental failure envelopes for buried surface hoar from displacement-controlled tests
- Our results suggest that an elliptical failure envelope conforms more closely to the data than a Mohr-Coulomb-cap model
- Buried surface hoar is weaker in shear than in compression (shear 1/3 to 2/3 comp. strength). Density alone is not a reliable predictor

Correspondence to:
J. Schöttner,
jakob.schoettner@slf.ch

Citation:
Schöttner, J., Piecuch, M., Rosendahl, P. L., Walet, M., Adam, V., Weißgraeber, P., et al. (2026). Testing the strength of buried surface hoar weak layers under combined compression and shear loading. *Geophysical Research Letters*, *53*, e2025GL120870. https://doi.org/10.1029/2025GL120870

Received 3 DEC 2025
Accepted 9 MAR 2026

Author Contributions:
Conceptualization: Jakob Schöttner, Philipp L. Rosendahl, Philipp Weißgraeber, Jürg Schweizer, Alec van Herwijnen
Data curation: Jakob Schöttner, Marcel Piecuch
Funding acquisition: Philipp L. Rosendahl, Alec van Herwijnen
Investigation: Marcel Piecuch, Melin Walet, Valentin Adam
Methodology: Jakob Schöttner, Philipp L. Rosendahl, Melin Walet, Valentin Adam, Philipp Weißgraeber, Jürg Schweizer, Alec van Herwijnen
Resources: Alec van Herwijnen
Supervision: Jakob Schöttner, Philipp L. Rosendahl, Jürg Schweizer, Alec van Herwijnen

Testing the Strength of Buried Surface Hoar Weak Layers Under Combined Compression and Shear Loading

Jakob Schöttner[1], **Marcel Piecuch**[1,2], **Philipp L. Rosendahl**[2], **Melin Walet**[1], **Valentin Adam**[1,2], **Philipp Weißgraeber**[3], **Jürg Schweizer**[1], **and Alec van Herwijnen**[1]

[1]WSL Institute for Snow and Avalanche Research SLF, Davos Dorf, Switzerland, [2]Institute for Structural Mechanics and Design, Darmstadt, Germany, [3]Chair of Lightweight Design, University of Rostock, Rostock, Germany

Abstract We experimentally determined the multiaxial strength of weak layers of buried surface hoar using displacement-controlled tests under combined normal and shear loading on a custom testing machine. We tested 63 samples from three different weak layers, with strengths ranging from 1 to 10 kPa with considerable scattering. While shear strength was lower than compressive strength (typically about one to two thirds), we did not observe the very low shear strengths implied by a Mohr-Coulomb-cap type of failure envelope. Instead, our data were better described by elliptical failure envelopes, consistent with numerical predictions for other weak layer types. Density and microstructural parameters were quantified from micro-computed tomography. Bulk density alone did not predict strength or envelope shape, but the data are not yet sufficient to derive robust quantitative structure–property relations. The envelope shape also appeared to be unrelated to the elastic properties, indicating that different microstructural aspects might govern elasticity and strength.

Plain Language Summary Snow avalanches start when a weak layer within the snowpack fails, but it is not well understood how these layers break under different directions of loading. One of the most fragile weak layers is buried surface hoar, which forms when delicate frost crystals on the snow surface are buried by new snow. On an inclined avalanche slope, the weight of the snow and, for example, the load of a skier can be decomposed into components normal and parallel to the slope, producing compression on the weak layer and shear along it. To better understand how these layers fail under such combined loading, we tested 63 snow samples in the laboratory using a custom-built machine that allowed precise control of the deformation. In our experiments, the weak layers were easier to break in shear than in compression. The failure behavior in stress space followed an elliptical pattern, which means that surface hoar can fail in pure shear, in pure compression, and in any combination of these two loading directions. These results improve our understanding of how avalanches start and can help to enhance avalanche forecasting in the future.

1. Introduction

Slope failures in soils, rocks, and snow share a common trigger: the loss of strength along a buried weakness that separates an intact body from its substrate. Whether in landslides, rock avalanches, or dry-snow slab avalanches, failure occurs when stress states at depth reach a critical loading. Predicting such events therefore requires understanding the geometry of the failure envelope—the surface in stress space that defines the transition from stable to unstable conditions. While this concept is well established in soil and rock mechanics, its form for snow, a highly porous and evolving geomaterial, remains poorly constrained.

In snowpacks, the weak layer beneath a slab is particularly fragile and often consists of faceted crystals, depth hoar, or surface hoar (Schweizer et al., 2003). It is subjected to multiaxial loading from the snowpack's self-weight and external perturbations such as skiers or a snowfall. In a slope-aligned coordinate system, this loading is commonly expressed as normal and shear components acting on the weak layer plane, which are not necessarily aligned with the principal stress directions and can vary substantially with snowpack stratigraphy and loading conditions even for similar slope angles. The relevant descriptor is the multiaxial failure envelope, which links normal- and shear stress to delineate stable from failing states.

For isotropic materials, invariant-based formulations in Haigh–Westergaard space (I_1, J_2, and J_3) provide a compact representation of the failure surface. Here, I_1 defines the hydrostatic axis. The deviatoric plane is described by the deviatoric radius ρ (proportional to $\sqrt{J_2}$) and the Lode angle Θ (a function of $J_3/J_2^{3/2}$), where J_2 and J_3 are the second and third invariants of the deviatoric stress. Meridian sections along the hydrostatic axis then

Writing – original draft: Jakob Schöttner, Marcel Piecuch, Philipp L. Rosendahl, Melin Walet, Valentin Adam, Philipp Weißgraeber, Jürg Schweizer, Alec van Herwijnen

quantify pressure sensitivity, while π-plane sections orthogonal to the hydrostatic axis reveal Lode dependence of strength (Bigoni & Piccolroaz, 2004; Christensen, 2013; Hach et al., 2026; Lode, 1926; Rosendahl, Kolupaev, & Altenbach, 2019). Classical criteria map to simple shapes in this space: von Mises (J_2-only cylinder around the hydrostatic axis), Drucker-Prager (I_1–J_2 cone centered around the hydrostatic axis), and Mohr–Coulomb (frictional pyramid), with cap-type extensions often introduced to ensure closure at high confinement (Chen & Zhang, 1991; Coulomb, 1773; Drucker & Prager, 1952; Mohr, 1900; Rosendahl, Staudt, et al., 2019). Such formulations are commonly used to reduce multiaxial stress states to an equivalent stress (to be compared with material strength) or, when several parameters are needed to describe the failure surface Φ, to define linear failure indices along the loading path (Hach et al., 2026). For the slab–weak layer configuration considered here, normal and shear stresses dominate, so we describe the failure envelope in the σ–τ plane, which provides a practical section of the broader failure surface because other multiaxial loading configurations are difficult to realize experimentally. In this sense, our representation can be viewed as a physically meaningful 2D slice of Φ that reflects pressure sensitivity and compressive failure through I_1 (Gibson & Ashby, 1997; Rosendahl, Drass, et al., 2019), and shear dependence through J_2 (Chen & Zhang, 1991; Christensen, 2013).

Despite extensive testing, the geometry of the weak layer failure envelope is still poorly constrained. Most studies measure strength in a single dominant loading mode, either compression or shear (e.g., de Montmollin, 1982 Föhn et al., 1998; Fukuzawa & Narita, 1993;; Jamieson & Johnston, 2001; Jamieson & Schweizer, 2000; Schöttner, Zeller-Plumhoff, et al., 2026; Schöttner et al., 2025; Schweizer, 1998), while only few studies span the combined σ–τ domain (e.g., Chandel et al., 2014; Jamieson and Johnston, 1998; McClung, 1977; Nakamura et al., 2010; Reiweger et al., 2015; Zeidler and Jamieson, 2006). Methodological heterogeneity, such as differences in sample type, preparation, density, and loading rate further limits comparability.

Experimental and numerical studies suggest two recurring families of envelope shapes: conic-section–like surfaces (ellipses, parabolas, …) (e.g., Blatny et al., 2021; Bobillier et al., 2020; Chandel et al., 2014; Ritter et al., 2020) and Mohr–Coulomb–cap–type surfaces (e.g., Chandel et al., 2015, 2014; Gaume et al., 2014; Jamieson and Johnston, 1998; McClung, 1977; Nakamura et al., 2010; Reiweger et al., 2015). Several studies also report intermediate or blended forms (e.g., Chandel et al., 2015; Gaume et al., 2014; Mulak and Gaume, 2019; Mede et al., 2018). The choice of envelope shape affects how failure is represented under combined normal and shear stresses and influences modeling outcomes. The limited experimental multiaxial coverage and methodological heterogeneity outlined above underscore the need for systematic, controlled, coupled compression and shear experiments across a broad σ–τ domain.

Here we conduct displacement-controlled multiaxial tests on natural buried surface hoar layers using a custom-built apparatus. We probe the failure envelope from compression-dominated to shear-dominated regimes, quantify its geometry and associated parameters, and compare the results with prior experimental and numerical studies to assess which type of envelope shape is more consistent with the observations. The results constrain the multiaxial strength of weak layers and provide essential parameters for physics-based avalanche-release simulations.

2. Methods

2.1. Snow Weak Layer Samples

Samples including surface hoar weak layers were harvested in February 2024 and February 2025 in the Flüela Valley near Davos, Switzerland, at about 1,640 m a.s.l. The sampling site was the flat, shaded roof of a bunker near a creek, where a horizontally layered snowpack and minimal solar radiation until early February favors regular surface hoar formation. Snow blocks ("parent samples") of approximately 60 × 40 cm^2 were cut with a snow saw, placed in polystyrene boxes, and stored at −20°C in the cold laboratory. The snow layers surrounding the weak layer consisted of rounded grains and decomposed particles. The SH24 and SH25.1 samples also exhibited a melt-freeze crust directly above the weak layer. Ten parent samples were obtained in 2024 and eight in 2025; since two weak layers were present in 2025, the 2025 blocks were split horizontally, yielding three series: SH24, SH25.1, and SH25.2. All samples were tested in May–June 2025.

2.2. Experimental Setup and Testing Procedure

The experiments were performed in a displacement-controlled, biaxial testing machine at −5(±1) °C (Schöttner et al., 2024). 1 day before testing, up to four specimens ($10 \times 20 \times 15\ \mathrm{cm}^3$) were cut from each parent sample and freeze-bonded on their top and bottom faces to pre-cooled, 3D-printed holders using a thin water film. The holders provided a rigid interface for direct displacement transfer. Because both interfaces had to be attached to the machine force-locked and without play, completely stress-free mounting was not possible. Residual force offsets were quantified from baseline measurements without a sample and removed in post-processing. During the experiment, the vertical actuator applied compression to the top of the sample, and the horizontal actuator moved the bottom sideways, yielding superimposed unconfined compression and simple shear. The relative actuator displacement rates prescribed the displacement angle θ_{xy}, which set the normal–shear partition for each test. Each machine axis was driven by a linear motor and guided by linear rails, instrumented with a high-precision load cell (1 kN capacity, 0.1 N resolution) and linear encoders. Data were sampled at 1,000 Hz. The upper plate allowed a ±5° tilt for alignment with the sample and could be locked with three thumb screws.

Displacement-controlled tests under combined normal and shear loading require careful consideration because the shear modulus G is typically smaller than the elastic modulus E. As a result, identical normal (y) and shear (x) displacements do not generate comparable stress responses (e.g., Luo et al., 2021; Vogler et al., 2000; Xu and Dai, 2018). Hence, the machine's prescribed displacement ratio (expressed as the displacement angle $\theta_{xy} = \arctan(u_x/u_y)$) generally differs from the reaction force angle $\varphi_{xy} = \arctan(F_x/F_y)$, and thus from the resulting normal and shear stresses (see Figure 1a). To span the full range of σ–τ conditions, we therefore applied proportionally larger horizontal (shear) displacements.

The required displacement ratios were obtained from a finite-element (FEM) parameter study of a three-layer linear-elastic model (slab–weak layer–slab) in ANSYS Mechanical (static structural, Mechanical APDL solver). The model was meshed with 3D solid elements using a uniform element size of 5 mm; the bottom surface was fixed and horizontal displacements were prescribed at the top surface according to the displacement angle θ_{xy}. Reaction forces were used to derive φ_{xy}. The study spanned Poisson's ratios $\nu \in [0.1, 0.4]$ and elastic modulus ratios $E_{\mathrm{wl}}/E_{\mathrm{slab}} \in [0.1, 1.0]$ ($N = 760$), and the resulting mapping $\varphi_{xy} \mapsto \theta_{xy}$ is shown in Figure 1b.

Deformation of the samples was recorded with a Phantom Veo 710L high-speed camera (AMETEK Vision Research, USA–1,280 px × 720 px) at 1,000 frames per second, mounted 60 cm from the rig and synchronized to the mechanical data via a trigger signal. To enhance contrast for digital image correlation (DIC), specimens were speckled with black ink (Figure 1a).

2.3. Data Post-Processing and Evaluation

We recorded mechanical- and high-speed video data of the experiment simultaneously, until after the moment of failure. The machine measured compressive and shear forces, temperature, relative humidity, and trigger signals at 1,000 Hz, providing the primary data for characterizing the multiaxial behavior of the weak layers. The raw force signals were filtered using a second-order low-pass Bessel filter with a 10 Hz cutoff to reduce noise (Virtanen et al., 2020). Compressive and shear stresses (σ and τ) were obtained by dividing the respective filtered forces (F_x and F_y) by the horizontal cross-sectional area of the sample $\left(20 \times 10\ \mathrm{cm}^2\right)$, which defines the relevant area for both types of stress.

To obtain accurate strain information for the weak layer alone, high-speed video recordings were analyzed using DIC software (DICe; Turner et al., 2015). Full-field strain measurements within the weak layer were unreliable: the highly porous microstructure induces depth-of-field effects, individual crystals deform in a complex manner, and post-failure disturbance of crystal fragments compromises correlation quality and strain estimates. Instead, we tracked the speckle pattern in two long and thin rectangular regions of interest (ROIs) placed immediately above and below the weak layer in order to calculate the effective displacement in the weak layer (white horizontal regions in Figure 1a). From each ROI, the average horizontal (u_x) and vertical (u_y) displacements as well as the rigid body rotation $\left(\beta_z\right)$ were obtained. Due to the finite stiffness of the machine and the sample attachment, a small but systematic rigid-body rotation about the out-of-plane axis was present in most experiments (mean rotation at failure $\bar{\beta}_z \approx 0.03°$, with maxima up to $\approx 0.3°$ in tests with the largest shear contributions). To isolate the layer deformation, we corrected the relative displacements between the upper and lower ROIs for rigid-body

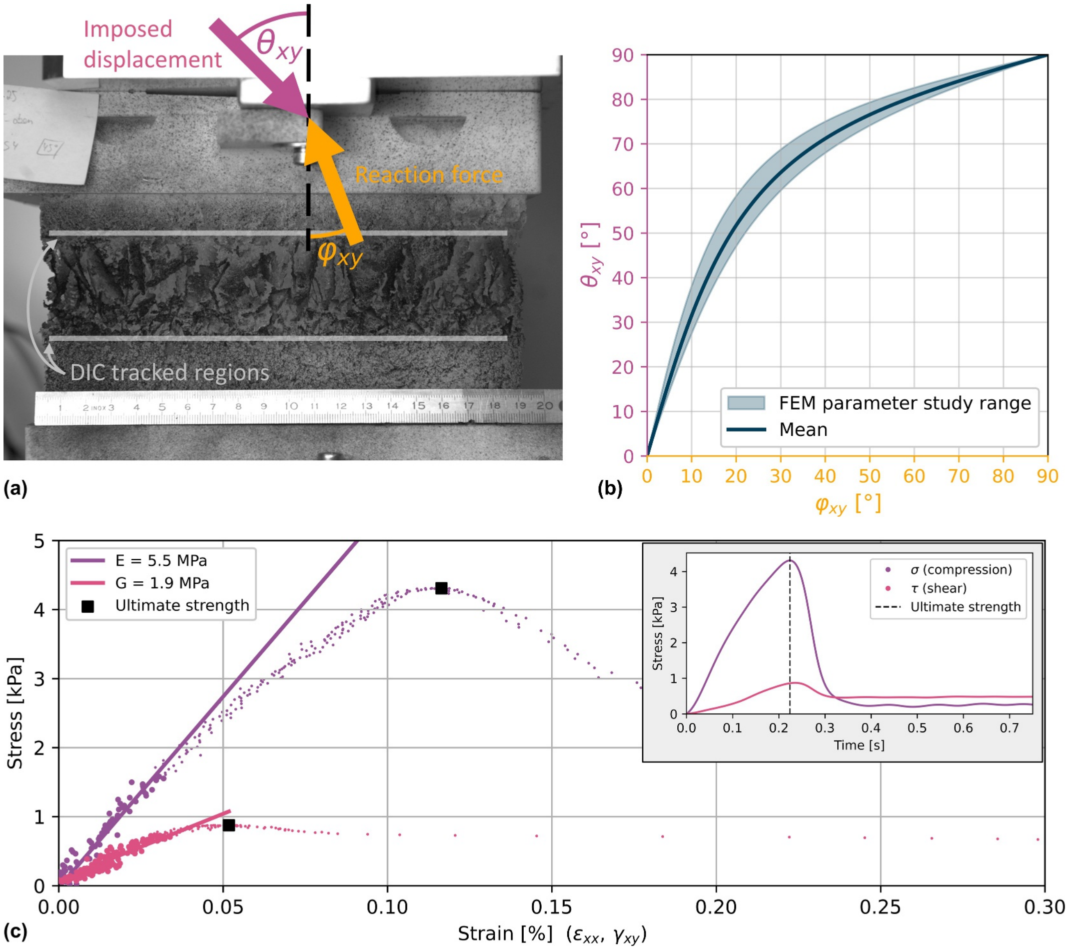

Figure 1. (a) Weak layer specimen in the biaxial testing machine, speckled with black ink to improve image contrast, illustrating the imposed displacement angle θ_{xy} and the resulting reaction-force angle φ_{xy}. The weak layer is defined by the ~4 cm thick surface hoar layer visible in the image. Displacement of the white horizontal regions was tracked using digital image correlation to quantify strain within the weak layer. (b) FEM-based mapping $\varphi_{xy} \mapsto \theta_{xy}$ for a three-layer system (slab–weak layer–slab). The shaded band spans $\nu \in [0.1, 0.4]$ and $E_{\mathrm{wl}}/E_{\mathrm{slab}} \in [0.1, 1.0]$ ($N = 760$ parameter combinations); the solid line shows the mean relation. (c) Example of the measured stress–strain response for a test with $\theta_{xy} = 30°$. Dots show normal stress σ (compression) and shear stress τ as a function of compressive strain ε_{xx} and engineering shear strain γ_{xy}. Square markers indicate the ultimate normal and shear strength. The straight line segments indicate how the elastic modulus E and shear modulus G were obtained, with the data points used for the fits highlighted. The corresponding stress–time signals are included to indicate when these features occur during loading. For this specimen, the extracted ultimate strengths correspond to a reaction-force angle $\varphi_{xy} \approx 12.5°$.

rotation of the sample using a small-angle approximation for the rotation (Schreier et al., 2009). Compressive strain (ε_{yy}) and engineering shear strain (γ_{xy}) across the weak layer were then computed as:

$$\varepsilon_{yy} = \frac{\Delta u_y + \beta_z\,\Delta x}{h_{\mathrm{wl}}}, \qquad \gamma_{xy} \equiv 2\varepsilon_{xy} = \frac{\Delta u_x + \beta_z\,\Delta y}{h_{\mathrm{wl}}}. \tag{1}$$

where Δu_x and Δu_y are the translational displacement differences between the ROIs in horizontal and vertical direction (still containing rigid-body rotation), Δx and Δy are the horizontal and vertical offsets between the ROI centroids (with $\Delta y \approx h_{\mathrm{wl}}$), β_z is the measured rigid body rotation in radians, and h_{wl} denotes the weak layer thickness, which is the relevant length for the calculation of both types of strain. Camera calibration minimized lens distortion and enabled accurate conversion from pixels to millimeters, while synchronization with the machine data was ensured via a trigger signal.

Failure was clearly visible in the stress–strain signals as a sudden drop in stress (see Figure 1c). We defined the failure point as the time when the magnitude of the stress vector reached its maximum, just before this drop. The normal and shear stresses at that time were taken as the compressive and shear strength, respectively.

The stress-strain signals were also used to estimate the elastic response and the strain rate of the experiment. To this end, we analyzed the linear region of the stress-strain plots using an incremental regression approach, necessary because of the relatively high amounts of noise in the data. We fitted a regression line to the first 10% of the linear region and added further data points until $R^2 \geq 0.9$ was fulfilled, as described in detail in Schöttner, Zeller-Plumhoff, et al. (2026). Fits that did not meet this criterion were not considered. This procedure is illustrated in Figure 1c. We then used the resulting mean elastic $\bar{E}$ and shear $\bar{G}$ modulus per weak layer to estimate the Poisson's ratio according to:

$$\bar{\nu} = \frac{\bar{E}}{2\bar{G}} - 1. \tag{2}$$

Values of $\bar{\nu}$ with $\bar{\nu} \notin (-1, 0.5)$, that is outside the physically admissible range for linear isotropic elasticity, are marked with an $*$. We retain them only as an indicator of the E–G ratio and the magnitude of this deviation.

In addition to the mechanical tests, we obtained microstructural information using micro-computed tomography (μCT). For this purpose, one weak layer sample was extracted from each parent sample and scanned in an 80 mm sample holder at a resolution of 29.1 μm. The resulting scans were post-processed and analyzed using standard methods (Schöttner, Zeller-Plumhoff, et al., 2026).

3. Results

In total, we performed approximately 80 experiments under loading conditions ranging from simple shear to pure compression. Of these, 63 samples yielded usable data; the remaining tests were discarded due to specimen damage during mounting or at the sample holder interface, or clearly invalid measurement signals. In parallel, we conducted 20 μCT scans of all parent samples to obtain detailed density information and a comprehensive set of standard microstructural metrics.

To verify the experimental conditions, we first address the *strain rate*, a parameter to which snow's mechanical properties are highly sensitive. The strain rate was estimated from the linear regions of the stress–strain curves and the corresponding time signals. The average strain rate components in the weak layer were $\dot{\varepsilon}_{yy} = 1.1(\pm 1.8) \times 10^{-3}\ \mathrm{s}^{-1}$ in compression and $\dot{\gamma}_{xy} \equiv 2\dot{\varepsilon}_{xy} = 2.0(\pm 1.4) \times 10^{-3}\ \mathrm{s}^{-1}$ in shear. These values place our experiments in the quasi-brittle regime (e.g., Löwe et al., 2020), although the stress–strain curves indicate some degree of plastic deformation preceding failure.

Figure 2a summarizes the *effective, linear-elastic properties* obtained from these experiments. The amount of usable data was further reduced by about a third, as many stress–strain signals were affected by noise. In particular, for tests dominated by compressive loading, it was difficult to reliably determine G, whereas for those with a high proportion of shear loading, deriving E proved challenging. The resulting mean elastic $E = \sigma/\varepsilon_{yy}$ and shear $G = \tau/\gamma_{xy}$ moduli were $E = 9.16(\pm 5.6)$ MPa and $G = 3.65(\pm 2.3)$ MPa for SH24, $E = 9.08(\pm 4.4)$ MPa and $G = 4.05(\pm 1.4)$ MPa for SH25.1, and $E = 12.47(\pm 3.7)$ MPa and $G = 3.44(\pm 1.1)$ MPa for SH25.2. Assuming isotropic material behavior, the corresponding mean Poisson's ratios are $\bar{\nu} = 0.26$, 0.12, and 0.81^*, respectively. We note that snow is generally anisotropic, so these values are effective parameters obtained under a commonly used isotropic approximation for snow.

Considerable scatter was observed in the *ultimate strength* data, which are shown in the τ–σ plane in Figure 2b to represent the proportions of shear and compressive stress at failure. Nevertheless, shear strength was generally lower than compressive strength. We did not observe the pronounced frictional trend implied by Mohr-Coulomb-cap criteria; instead, our data support a conic-section–like failure surface, which seems to be well described by a simple, elliptical failure envelope in the shape of:

$$\left(\frac{\sigma}{\sigma_c}\right)^2 + \left(\frac{\tau}{\tau_c}\right)^2 = 1, \tag{3}$$

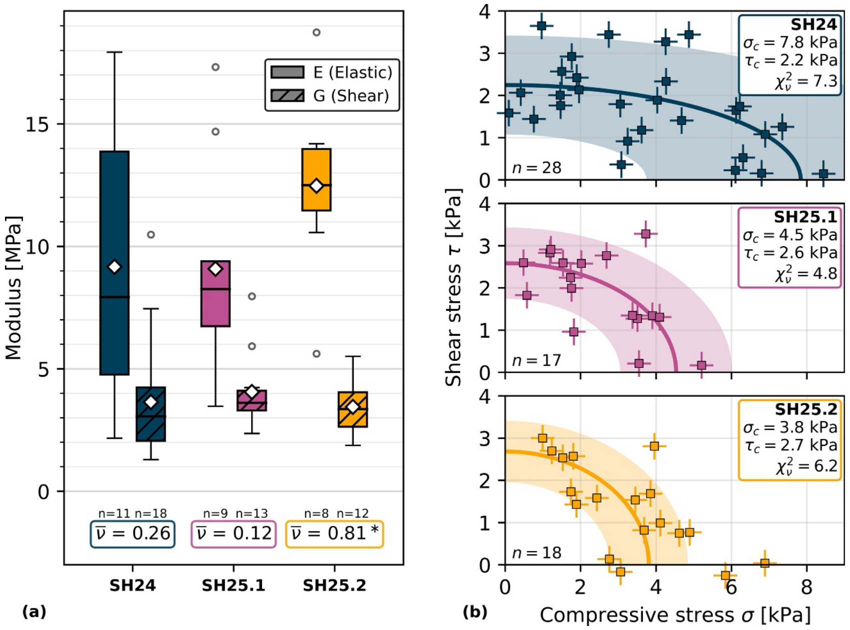

Figure 2. Overview of experimental results: (a) Measured effective elastic modulus E and shear modulus G shown as box plot, with boxes indicating the interquartile range and whiskers the full data range. The horizontal bar marks the median, and the diamond symbol denotes the mean value. The theoretical Poisson's ratio $\bar{\nu}$ is calculated from the mean values of E and G assuming isotropic material behavior. (b) Ultimate strength values obtained from the experiments shown in the τ–σ plane, including the resulting elliptical failure envelopes and the 1σ prediction bands. The reduced χ^2 values $(\chi^2_\nu \in [4.8, 7.3])$ exceed unity, indicating scatter beyond measurement uncertainty.

with only two free parameters σ_c, τ_c being the points where the envelope intersects the σ and τ-axis. We used an orthogonal distance regression (ODR–Boggs and Rogers, 1990) for the fitting.

The resulting τ_c values were nearly identical for all samples, ranging between 2.2 and 2.7 kPa. In contrast, the σ_c values differed more markedly: while SH25.1 and SH25.2 showed similar values of 4.5 and 3.8 kPa, the SH24 weak layer reached a considerably higher value of 7.8 kPa, roughly twice that of the 2025 samples. This indicates that SH24 was more resistant to compressive loading.

Microstructural characteristics derived from µCT analysis are shown in Figure 3. The bulk densities of the weak layers were 177(± 23) kg m^{-3} for SH24, 166(± 34) kg m^{-3} for SH25.1, and 102(± 9) kg m^{-3} for SH25.2. The corresponding weak layer heights were 10.4(± 1.6) mm for SH24, 13.6(± 1.6) mm for SH25.1, and 31.6(± 3.8) mm for SH25.2. Among these, SH24 exhibited substantially higher minimum densities (Figure 3d) despite having a bulk density comparable to SH25.1. Specific surface area (SSA$_{\mathrm{ice}}$ - Figure 3e), vertical anisotropy (Figure 3f), and vertical tortuosity (Figure 3h) were of similar magnitude across all three weak layer types. Local thickness analysis (Figure 3g), however, revealed clear distinctions: SH24 showed the lowest values in both ice and pore thickness, indicating a network of fine ice structures with limited pore space. SH25.1 displayed nearly identical pore thickness but greater variability in ice thickness, whereas SH25.2 exhibited the opposite trend, with uniform ice thickness and more variable pore geometry. Interfacial curvature analysis further highlighted systematic differences. SH24 and SH25.1 exhibit a broad spread in both mean and Gaussian curvature, whereas the SH25.2 samples cluster more tightly (Figure 3i).

4. Discussion

We tested 63 samples from three weak layers of buried surface hoar under combined simple shear and unconfined compression to determine their failure envelopes. Here, we discuss the findings with attention to experimental influences, microstructure, relevant literature, and key limitations.

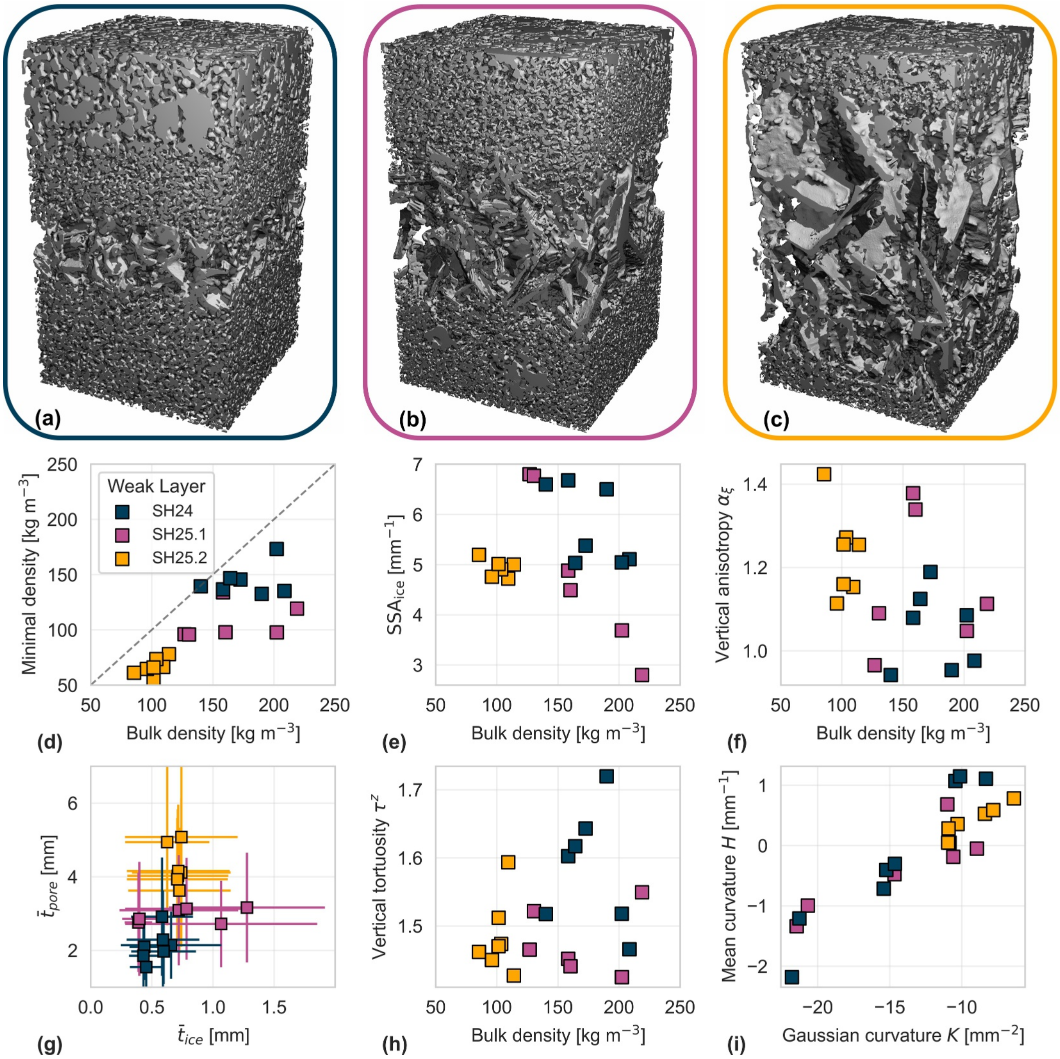

Figure 3. Summary of key microstructural parameters. (a–c) show 3D renderings of the three tested weak layers SH24 (177(±23) kg m^{-3}), SH25.1 (166(±34) kg m^{-3}), and SH25.2 (102(±9) kg m^{-3}), respectively (section size: $3 \times 3 \times 5$ cm^3). (d–i) compare key microstructural parameters according to Schöttner, Zeller-Plumhoff, et al. (2026).

4.1. Experimental Setup

We used a displacement-controlled device to perform multiaxial tests on natural buried surface hoar under well-defined laboratory conditions, to our knowledge, the first implementation of this kind. From these tests, we derived mechanical properties and failure envelopes. The results show considerable scatter, which we partly attribute to natural variability in sample properties, most notably density, within specimens from the same weak layer.

Two characteristics of the setup are important for interpreting the data. First, the strain rate in shear was, on average, about twice the compressive strain rate. However, since we report engineering shear strain rate ($\dot{\gamma}_{xy} = 2\dot{\varepsilon}_{xy}$), this difference is expected and does not imply a shear-dominated stress path. Overall, the applied rates place the tests in a quasi-brittle regime, although some stress–strain curves exhibited limited pre-failure plasticity. Second, finite stiffness of the frame and attachments resulted in small rigid-body rotations of the specimen. We corrected the ROI displacements for this effect; without correction, elastic properties would be underestimated by ≈ 5% in E and ≈ 53% in G. The large effect on G follows from the ROI geometry: their centers are aligned in x but separated in y by the weak layer thickness $\Delta y \approx h_{\text{wl}}$. A small rotation β_z induces a substantial relative x-shift $\Delta u_x \approx \beta_z\,\Delta y$, which contaminates the apparent engineering shear strain γ_{xy}, while the normal strain ε_{yy} is largely unaffected; hence G is far more sensitive to rotation than E.

4.2. Experimental Data: Effective Elastic Properties

Estimating effective elastic parameters proved challenging and produced substantial scatter because the data set is relatively small and only a subset of tests yielded usable signals. Under predominantly compressive loading, the shear modulus could not always be extracted, and vice versa. Nevertheless, approximate values of the effective elastic modulus E and the effective shear modulus G were obtained, allowing us to estimate Poisson's ratios $\bar{\nu}$ under the assumption of isotropy. The inferred Poisson's ratios (0.26, 0.12, and 0.81*) indicate pronounced mechanical heterogeneity across weak layers. The first value falls within typical ranges reported or estimated for snow weak layers (e.g., Adam et al., 2024; Mellor, 1975; Weißgraeber and Rosendahl, 2023); the second is rather small, and the third exceeds the isotropic upper bound ($\nu \leq 0.5$), inconsistent with a homogeneous, linear-elastic continuum. This suggests that some weak layers may not be well represented by a single bulk parameter set; instead, their macroscopic elastic response might be governed by microstructural architecture (akin to metamaterials) where microstructure governs the mechanical behavior. Given the limited number of elastic data sets and the noise sensitivity of modulus identification, these values should be interpreted as indicative rather than definitive.

The measured E values were of the same order of magnitude as in Schöttner, Zeller-Plumhoff, et al. (2026) but tended to be on the higher side at comparable bulk densities. We attribute this to microstructural differences: the present samples exhibited higher minimal densities and distinct microstructural metrics relative to the earlier data set. For G, experimental benchmarks for surface hoar weak layers are scarce; to our knowledge, only Föhn et al. (1998) reported shear moduli of about 0.3 MPa for weak layers with shear strength around 1.5 kPa, at much higher strain rates on the order of $10^{-1}\ \mathrm{s}^{-1}$. This is about one order of magnitude lower than the values we found, though a direct comparison is difficult. We also tested whether the parameterization of Sundu et al. (2024) for snow elasticity applies to buried surface hoar microstructures. It predicted low Poisson's ratios ($\nu \approx 0.10$–0.15), while the corresponding E and G differed from our measurements by up to about a factor of five, without a clear systematic trend.

4.3. Experimental Data: Strength and Failure Envelopes

Our data support conic-section-like representations of the failure surfaces for buried surface hoar weak layers. We found no evidence for Mohr-Coulomb-cap behavior, such as a frictional cut-off or a systematic increase of shear strength with added compression. We fitted elliptical envelopes because they provide a compact, physically motivated description that captures the overall trend of the data and is consistent with prior work. We emphasis that this choice is not intended to imply an optimal solution, but rather to provide a concise representation of the central tendency in our measurements. The reduced χ^2 values $\left(\chi^2_\nu \in [4.8,\ 7.3]\right)$ exceed unity, indicating scatter beyond measurement uncertainty and pointing to experimental variability and/or sample heterogeneity.

To ground the discussion, we first compare strength magnitudes via the axis intercepts σ_c and τ_c obtained from the fits. Our data were in the range of $\sigma_c = 3.8$–7.8 kPa and $\tau_c = 2.2$–2.7 kPa, broadly consistent with published ranges for buried surface hoar yet slightly higher than previously reported values (Chandel et al., 2023; Föhn et al., 1998; Jamieson & Johnston, 2001; Nakamura et al., 2010; Reiweger & Schweizer, 2010; Schöttner, Zeller-Plumhoff, et al., 2026). The difference $(\sigma_c > \tau_c)$ confirms comparatively low shear strength, though not as low as often assumed (e.g., Perla et al., 1983).

While elliptical envelopes are supported by a broad literature, particularly numerical studies, it is difficult to assess our results against *experimental* multiaxial data for buried surface hoar because such data sets are scarce. We provide a detailed overview comparing our envelope shapes to experimental and numerical literature data in Figure 4, but for the discussion focus on Reiweger et al. (2015), Chandel et al. (2023), and Jamieson and Johnston (1998), to our knowledge the only experimental studies that investigated surface hoar strength under combined loading. Reiweger et al. (2015) and Chandel et al. (2023) report low nominal strain rates; however, compliance at the machine–snow interface can make the in-specimen rate lower than reported (Schöttner et al., 2025). For Jamieson and Johnston (1998), compression was applied quasi-statically by placing dead weights on the shear frame (effectively load-controlled), and no explicit strain rates are reported for shear.

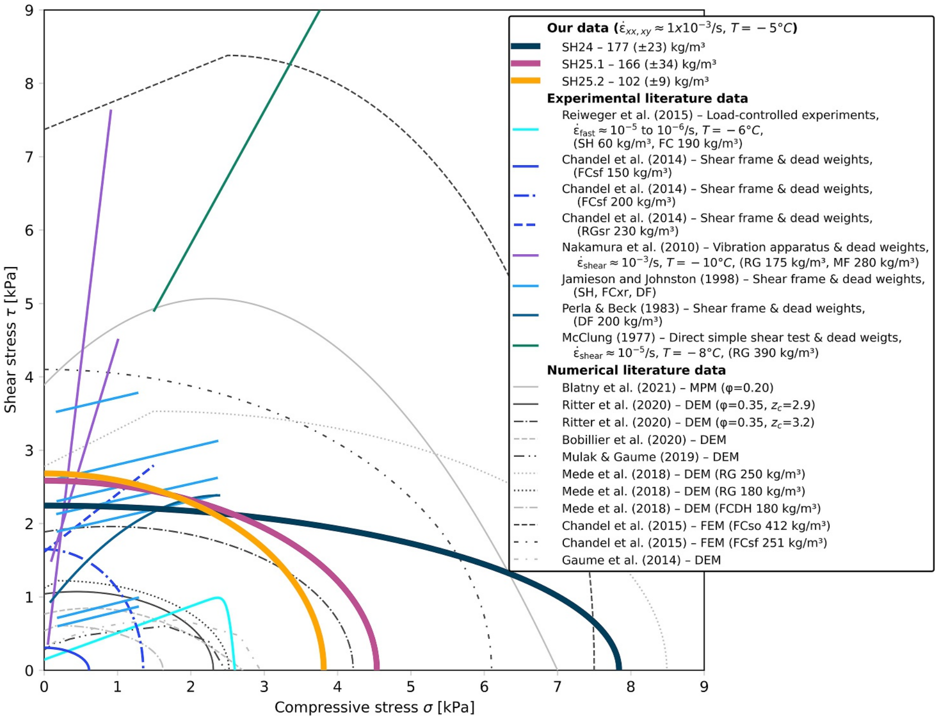

Figure 4. Comparison of our failure envelopes with a non-exhaustive selection of experimental and numerical results from the literature, including snow types (according to Fierz et al. [2009]) and experimental conditions. Literature envelopes are reproduced as reported and were not rescaled (e.g., to account for density differences); the comparison is therefore intended to highlight envelope shape rather than absolute values.

For Chandel et al. (2023), the reported strengths (0.6–2.2 kPa) are lower than ours, consistent with their lower weak layer density $\left(\approx 45\ \text{kg}\,\text{m}^{-3}\right)$. The precise locations of these data points in the σ–τ plane are uncertain; our FEM analysis (Figure 1) indicates that a 45° weak layer orientation under uniaxial compression generates only a small shear stress component (loading angle $\varphi_{xy} \approx 10$–$20°$), that is, a predominantly normal loading state. Overall, their results are consistent with our envelopes.

By contrast, we cannot reconcile the trend reported by Reiweger et al. (2015) and Jamieson and Johnston (1998) with our results. We did not observe a comparable increase of shear strength with compression and do not have a robust hypothesis for this discrepancy. In particular, Reiweger et al. (2015) combined a broad range of densities and crystal types into a single curve; our data and our earlier study (Schöttner, Zeller-Plumhoff, et al., 2026) did not show a comparable collapse for brittle weak layers. Because multiaxial testing of snow is inherently difficult, the stress state and boundary conditions may have been imperfectly constrained despite best efforts, potentially affecting the inferred envelopes (ASTM International, 2019). Even with our displacement-controlled apparatus, designed to limit such effects, we observed small rigid-body rotations, underscoring the sensitivity of results to experimental control. The extreme increase in shear strength with compressive loading reported by Nakamura et al. (2010) may not reflect brittle weak layer behavior and may involve additional processes; McClung (1977) did not probe the brittle regime and is therefore not directly comparable. We refrain from attributing discrepancies to specific setups and instead emphasize the need for careful stress-state control and video analysis in future work.

4.4. Influence of Snow Microstructure

Microstructural analyses served both to establish accurate densities and to probe microstructural controls on strength. For our fits, density was not a reliable predictor of either absolute strength or failure envelope shape. SH25.1 and SH25.2 displayed nearly identical envelopes despite a mean density difference of $\approx 65\ \text{kg}\,\text{m}^{-3}$, whereas SH24 and SH25.1 had comparable densities but clearly different envelopes, with SH24 showing roughly twice the compressive strength. Taken together, these contrasts suggest that, in addition to bulk density, other microstructural attributes are likely important for the mechanical response.

Within the set of bulk microstructural metrics we measured, no single parameter emerged as a definitive predictor of envelope shape; nevertheless, several consistent patterns are evident. Minimum density (a proxy for the weakest portion of the layer) separated the series more clearly than bulk density (Figure 3d). Local thickness metrics also differentiated the layers: ice- and pore-thickness distributions varied in distinct ways across the series (Figure 3g). Topology metrics showed no trend; we suspect that strong vertical heterogeneity, evident in the gap between minimum and bulk density, masks potential signals when metrics are averaged over the layer. Interfacial curvature distributions differed as well, but irregular crystal morphologies hindered a direct mapping to bond-scale geometry. Overall, these patterns indicate that microstructure exerts first-order control on strength and envelope shape, whereas the present data set is not yet sufficient to derive robust quantitative structure–property relations.

A notable observation is a possible decoupling between strength trends in the $\sigma - \tau$ plane and the elastic properties. Across weak layers, the ratio σ_c/τ_c did not show a clear systematic relationship with E or G within the scatter of our elastic estimates. For example, SH24 exhibited substantially higher σ_c yet did not display clearly distinct values in E and, in particular, in ν. This tendency is consistent with our earlier findings on the role of snow microstructure (Schöttner, Zeller-Plumhoff, et al., 2026), suggesting that elastic properties and strength may be governed by *different* microstructural attributes. Further data are needed to test this hypothesis and to assess potential implications for the shape of the failure envelope.

A final consideration is material history. The SH24 weak layer was stored for more than 1 year at −20°C, allowing isothermal metamorphism and gravitational settling that could, in principle, modify its structure and strength. However, the same weak layer was already tested in compression in our previous study (Schöttner, Zeller-Plumhoff, et al., 2026, parent sample ID 577), at the time when the present specimens were harvested and put into storage. Comparing those earlier tests ($N = 8$) with the current SH24 measurements shows very similar compressive properties: $E_{\text{before}} = 10.53(\pm 6.6)$ MPa versus $E_{\text{after}} = 9.16(\pm 5.6)$ MPa, and $\sigma_{\text{before}} = 7.3(\pm 1.6)$ kPa versus $\sigma_{\text{after}} \approx \sigma_c = 7.8$ kPa. Within the experimental scatter, long-term storage at −20°C therefore does not appear to have altered the compressive response. At the same time, μCT-derived metrics (e.g., SSA) showed differences, indicating that the microstructure did evolve during storage. Notably, SH24 exhibited the highest compressive strength without a corresponding increase in shear strength relative to the 2025 layers. In light of reported time-dependent changes in shear strength of buried surface hoar layers (Jamieson & Schweizer, 2000), we cannot attribute this behavior unambiguously to either storage effects or initial microstructure.

4.5. Limitations

Several limitations should be considered when interpreting our findings: (a) *Sample state:* Short warm episodes in January 2024 and January 2025 caused brief isothermal conditions in all weak layers, so the tested samples may not span the full range of surface hoar microstructures. In SH24, flow channels were observed; samples visibly affected by liquid water were excluded. SH24 was also stored for over a year at −20°C, which may have altered its microstructure and contributed to its higher compressive strength. (b) *Sample size and trimming:* Sample dimensions varied by a few percent, and the cutting process may have damaged the outermost crystals. Both effects could lead to a slight underestimation of the true stresses, but this bias is expected to be small compared to the scatter in the data. (c) *Preload offsets:* Mechanical mounting introduced small preloads; true zero-force installation was not achievable. Offsets were estimated from empty control runs and are small relative to the overall scatter, but they remain a source of uncertainty, reflected in the error bars in Figure 2b. (d) *Elastic data set:* The number of usable elastic data is limited, and the identification of the moduli is noise-sensitive; larger sample sizes would improve the statistical robustness. In addition, we report effective elastic parameters under a isotropic approximation, although surface hoar is most likely anisotropic (e) *Microstructure representativeness:* μCT analysis relied on representative scans at the parent-sample level, preventing a sample-by-sample correlation between local structure and mechanical response. (f) *Sample rotation:* Small rigid-body rotations occurred despite careful alignment. Although we corrected for them in the DIC-based strain evaluation, they may still have slightly affected the measured forces. This highlights that accurate force measurements combined with in-sample displacement tracking using DIC are essential in mechanical snow experiments.

5. Conclusions and Outlook

We conducted displacement-controlled multiaxial tests on natural weak layers of buried surface hoar and derived failure envelopes spanning shear to compression. The data supports an elliptical formulation of failure envelopes, showing that normal and shear stresses interact to trigger failure, unlike most prior experimental reports. In our data set, bulk density did not show a clear relationship with strength or envelope shape. Instead, the mechanical response appears to depend on microstructure; yet, among the bulk microstructural descriptors we evaluated, no single dominant factor emerged. Our elastic estimates further suggest that, for some microstructures, a continuum description may be invalid.

Future work should expand multiaxial testing to other weak layer types while systematically varying key microstructural variables, so that robust structure-property relations can be established from a larger data set. Pairing each mechanical test with specimen-resolved μCT would then allow direct, sample-specific links between microstructure and mechanical response. Embedding these relationships in constitutive models should yield more reliable simulations of weak layer failure under realistic multiaxial loading and, ultimately could help to improve avalanche forecasting.

Conflict of Interest

The authors declare no conflicts of interest relevant to this study.

Availability Statement

The data set is available on EnviDat: https://www.doi.org/10.16904/envidat.684 (Schöttner, Piecuch, et al., 2026).

Acknowledgments

We thank L.F.M. da Silva, E. Marques, R. Carbas, C.M.S. Moreira da Silva, and I. Camacho for their contributions to the design and construction of the biaxial testing machine and their support during its commissioning and operation, as well as M. Jaggi and Lucid Concepts AG for their support in preparing and evaluating the μCT scans. We used deepl.com/write and chatgpt.com to enhance the language and readability of this manuscript. This research has been supported by the Swiss National Science Foundation (SNF) under Grant 201071 and German Research Foundation (DFG) under Grant 460195514. Open access publishing facilitated by ETH-Bereich Forschungsanstalten, as part of the Wiley - ETH-Bereich Forschungsanstalten agreement via the Consortium Of Swiss Academic Libraries.

References

Adam, V., Bergfeld, B., Weißgraeber, P., van Herwijnen, A., & Rosendahl, P. L. (2024). Fracture toughness of mixed-mode anticracks in highly porous materials. *Nature Communications*, *15*(1), 7379. https://doi.org/10.1038/s41467-024-51491-7

ASTM International. (2019). *Astm E1012-19: Standard practice for verification of testing frame and specimen alignment under tensile and compressive axial force application*. ASTM International. https://doi.org/10.1520/E1012-19

Bigoni, D., & Piccolroaz, A. (2004). Yield criteria for quasibrittle and frictional materials. *International Journal of Solids and Structures*, *41*(11–12), 2855–2878. https://doi.org/10.1016/j.ijsolstr.2003.12.024

Blatny, L., Löwe, H., Wang, S., & Gaume, J. (2021). Computational micromechanics of porous brittle solids. *Computers and Geotechnics*, *140*, 104284. https://doi.org/10.1016/j.compgeo.2021.104284

Bobillier, G., Bergfeld, B., Capelli, A., Dual, J., Gaume, J., van Herwijnen, A., & Schweizer, J. (2020). Micromechanical modeling of snow failure. *The Cryosphere*, *14*(1), 39–49. https://doi.org/10.5194/tc-14-39-2020

Boggs, P. T., & Rogers, J. E. (1990). Orthogonal distance regression. *Contemporary Mathematics*, *112*, 183–194.

Chandel, C., Mahajan, P., Srivastava, P. K., & Kumar, V. (2014). The behaviour of snow under the effect of combined compressive and shear loading. *Current Science*, *107*(5), 888–894.

Chandel, C., Srivastava, P. K., Kumar, V., Datt, P., Sheoran, R., & Satayawali, P. (2023). Laboratory set-up for surface hoar layer growth over rounded grain snow. *Cold Regions Science and Technology*, *205*, 103705. https://doi.org/10.1016/j.coldregions.2022.103705

Chandel, C., Srivastava, P. K., & Mahajan, P. (2015). Determination of failure envelope for faceted snow through numerical simulations. *Cold Regions Science and Technology*, *116*, 56–64. https://doi.org/10.1016/j.coldregions.2015.04.009

Chen, W. F., & Zhang, H. (1991). *Structural plasticity*. Springer New York. Retrieved from https://link.springer.com/book/9781461277460

Christensen, R. M. (2013). *The theory of materials failure*. Oxford University Press.

Coulomb, C. A. (1773). Essai sur une application des regles de maximis et minimis a quelques problemes de statique relatifs a l'architecture. *Memoires de Mathematique et de Physique, Academie Royale des Sciences*.

de Montmollin, V. (1982). Shear tests on snow explained by fast metamorphism. *Journal of Glaciology*, *28*(98), 187–198. https://doi.org/10.3189/s0022143000011898

Drucker, D. C., & Prager, W. (1952). Soil mechanics and plastic analysis or limit design. *Quarterly of Applied Mathematics*, *10*(2), 157–165. https://doi.org/10.1090/qam/48291

Fierz, C., Armstrong, R., Durand, Y., Etchevers, P., Greene, E., McClung, D., et al. (2009). *The international classification for seasonal snow on the ground. Paris: IHP-VII technical documents in hydrology N°83, IACS contribution N°1*. UNESCO-IHP.

Föhn, P. M., Camponovo, C., & Krüsi, G. (1998). Mechanical and structural properties of weak snow layers measured in situ. *Annals of Glaciology*, *26*, 1–6. https://doi.org/10.3189/1998aog26-1-1-6

Fukuzawa, T., & Narita, H. (1993). An experimental study on the mechanical behavior of a depth hoar layer under shear stress. In *Proceedings ISSW 1992. International Snow Science Workshop* (pp. 171–175).

Gaume, J., Chambon, G., Reiweger, I., van Herwijnen, A., & Schweizer, J. (2014). On the failure criterion of weak-snow layers using the discrete element method. In *Proceedings ISSW 2014. International Snow Science Workshop 2014, Banff, Canada*.

Gibson, L. J., & Ashby, M. F. (1997). *Cellular solids*. Cambridge University Press. https://doi.org/10.1017/CBO9781139878326

Hach, M., Radtke, A., & Weißgraeber, P. (2026). A linear failure index for the christensen criterion. *International Journal of Solids and Structures*, *324*, 113685. https://doi.org/10.1016/j.ijsolstr.2025.113685

Jamieson, B., & Johnston, C. D. (2001). Evaluation of the shear frame test for weak snowpack layers. *Annals of Glaciology*, *32*, 59–69. https://doi.org/10.3189/172756401781819472

Jamieson, J., & Johnston, C. (1998). Refinements to the stability index for skier-triggered dry-slab avalanches. *Annals of Glaciology*, *26*, 296–302. https://doi.org/10.3189/1998AoG26-1-296-302

Jamieson, J. B., & Schweizer, J. (2000). Texture and strength changes of buried surface-hoar layers with implications for dry snow-slab avalanche release. *Journal of Glaciology*, *46*(152), 151–160. https://doi.org/10.3189/172756500781833278

Lode, W. (1926). Versuche Über den Einfluß der mittleren Hauptspannung auf das Fließen der Metalle Eisen, Kupfer und Nickel. *Zeitschrift für Physik*, *36*(11–12), 913–939. https://doi.org/10.1007/BF01400222

Löwe, H., Zaiser, M., Mösinger, S., & Schleef, S. (2020). Snow mechanics near the ductile-brittle transition: Compressive stick-slip and snow microquakes. *Geophysical Research Letters*, *47*(4), e2019GL085491. https://doi.org/10.1029/2019GL085491

Luo, G., Xue, P., & Li, Y. (2021). Experimental investigation on the yield behavior of metal foam under shear-compression combined loading. *Science China Technological Sciences*, *64*(7), 1412–1422. https://doi.org/10.1007/s11431-020-1786-6

McClung, D. M. (1977). Direct simple shear tests on snow and their relation to slab avalanche formation. *Journal of Glaciology*, *19*(81), 101–109. https://doi.org/10.3189/S0022143000215578

Mede, T., Chambon, G., Hagenmuller, P., & Nicot, F. (2018). Snow failure modes under mixed loading. *Geophysical Research Letters*, *45*(24), 13351–13358. https://doi.org/10.1029/2018GL080637

Mellor, M. (1975). A review of basic snow mechanics. In *Symposium at Grindelwald 1974 - Snow mechanics* (Vol. 114, pp. 251–291).

Mohr, O. (1900). Welche Umstände bedingen die Elastizitätsgrenze und den Bruch eines Materials? *Zeitschrift des Vereines Deutscher Ingenieure*, *44*, 1524–1530.

Mulak, D., & Gaume, J. (2019). Numerical investigation of the mixed-mode failure of snow. *Computational Particle Mechanics*, *6*(3), 439–447. https://doi.org/10.1007/s40571-019-00224-5

Nakamura, T., Abe, O., Hashimoto, R., & Ohta, T. (2010). A dynamic method to measure the shear strength of snow. *Journal of Glaciology*, *56*(196), 333–338. https://doi.org/10.3189/002214310791968502

Perla, R., Beck, T., & Cheng, T. (1983). The shear strength index of alpine snow. *Cold Regions Science and Technology*, *6*(1), 11–20. https://doi.org/10.1016/0165-232X(82)90040-4

Reiweger, I., Gaume, J., & Schweizer, J. (2015). A new mixed-mode failure criterion for weak snowpack layers. *Geophysical Research Letters*, *42*(5), 1427–1432. https://doi.org/10.1002/2014GL062780

Reiweger, I., & Schweizer, J. (2010). Failure of a layer of buried surface hoar. *Geophysical Research Letters*, *37*(24), L24501. https://doi.org/10.1029/2010GL045433

Ritter, J., Löwe, H., & Gaume, J. (2020). Microstructural controls of anticrack nucleation in highly porous brittle solids. *Scientific Reports*, *10*(1), 12383. https://doi.org/10.1038/s41598-020-67926-2

Rosendahl, P., Drass, M., Felger, J., Schneider, J., & Becker, W. (2019). Equivalent strain failure criterion for multiaxially loaded incompressible hyperelastic elastomers. *International Journal of Solids and Structures*, *166*, 32–46. https://doi.org/10.1016/j.ijsolstr.2019.01.030

Rosendahl, P., Staudt, Y., Schneider, A., Schneider, J., & Becker, W. (2019). Nonlinear elastic finite fracture mechanics: Modeling mixed-mode crack nucleation in structural glazing silicone sealants. *Materials & Design*, *182*, 108057. https://doi.org/10.1016/j.matdes.2019.108057

Rosendahl, P. L., Kolupaev, V. A., & Altenbach, H. (2019). Extreme yield figures for universal strength criteria. In H. Altenbach & A. Öchsner (Eds.), *State of the art and future trends in material modeling* (1st ed., pp. 259–324). Springer. https://doi.org/10.1007/978-3-030-30355-6_12

Schöttner, J., Piecuch, M., Rosendahl, P. L., Walet, M., Adam, V., Weißgraeber, P., et al. (2026). Testing the strength of buried surface hoar weak layers under combined compression and shear loading [Dataset]. *EnviDat*. Retrieved from https://www.doi.org/10.16904/envidat.684

Schöttner, J., Walet, M., Marques, E., Carbas, R., Adam, V., Hohl, M., et al. (2024). Developing two multiaxial testing machines to link strength and microstructure of weak snow layers. In *Proceedings, International Snow Science Workshop 2024, Tromsø, Norway*.

Schöttner, J., Walet, M., Rosendahl, P., Weissgraeber, P., Adam, V., Walter, B., et al. (2025). On the compressive strength of weak snow layers of depth hoar. *Journal of Glaciology*, *71*, e54. https://doi.org/10.1017/jog.2025.16

Schöttner, J., Zeller-Plumhoff, B., Hagenmuller, P., Weißgraeber, P., Rosendahl, P. L., Löwe, H., et al. (2026). The influence of snow microstructure on the compressive mechanical properties of weak snowpack layers. *Acta Materialia*, *302*, 121657. https://doi.org/10.1016/j.actamat.2025.121657

Schreier, H., Orteu, J.-J., & Sutton, M. A. (2009). *Image correlation for shape, motion and deformation measurements*. Springer US. https://doi.org/10.1007/978-0-387-78747-3

Schweizer, J. (1998). Laboratory experiments on shear failure of snow. *Annals of Glaciology*, *26*, 97–102. https://doi.org/10.3189/1998AoG26-1-97-102

Schweizer, J., Jamieson, B., & Schneebeli, M. (2003). Snow avalanche formation. *Reviews of Geophysics*, *41*(4). https://doi.org/10.1029/2002RG000123

Sundu, K., Freitag, J., Fourteau, K., & Löwe, H. (2024). A microstructure-based parameterization of the effective anisotropic elasticity tensor of snow, firn, and bubbly ice. *The Cryosphere*, *18*(4), 1579–1596. https://doi.org/10.5194/tc-18-1579-2024

Turner, D., Crozier, P., & Reu, P. (2015). *Digital image correlation engine*. [Tech. Rep.]. National Technology & Engineering Solutions of Sandia, LLC (NTESS).

Virtanen, P., Gommers, R., Oliphant, T. E., Haberland, M., Reddy, T., Cournapeau, D., et al. (2020). SciPy 1.0: Fundamental algorithms for scientific computing in python. *Nature Methods*, *17*(3), 261–272. https://doi.org/10.1038/s41592-019-0686-2

Vogler, T., Hsu, S.-Y., & Kyriakides, S. (2000). Composite failure under combined compression and shear. *International Journal of Solids and Structures*, *37*(12), 1765–1791. https://doi.org/10.1016/S0020-7683(98)00323-0

Weißgraeber, P., & Rosendahl, P. L. (2023). A closed-form model for layered snow slabs. *The Cryosphere*, *17*(4), 1475–1496. https://doi.org/10.5194/tc-17-1475-2023

Xu, Y., & Dai, F. (2018). Dynamic response and failure mechanism of brittle rocks under combined compression-shear loading experiments. *Rock Mechanics and Rock Engineering*, *51*(3), 747–764. https://doi.org/10.1007/s00603-017-1364-2

Zeidler, A., & Jamieson, B. (2006). Refinements of empirical models to forecast the shear strength of persistent weak snow layers PART A: Layers of faceted crystals. *Cold Regions Science and Technology*, *44*(3), 194–205. https://doi.org/10.1016/J.COLDREGIONS.2005.11.005